Journal Name

Dynamic Article Links ►

Cite this: DOI: 10.1039/c0xx00000x

www.rsc.org/xxxxxx

ARTICLE TYPE

# The stability of thin polymer films as controlled by changes in uniformly sputtered gold

**George Amarandei,*[a] Colm O'Dwyer[b,c] , Arousian Arshak[a] and David Corcoran[a]**

***Received (in XXX, XXX) Xth XXXXXXXXX 20XX, Accepted Xth XXXXXXXXX 20XX***

**DOI: 10.1039/b000000x**

The stability of polystyrene thin films of low molecular weight on a solid substrate is shown to be controlled by the presence of uniformly distributed gold sputtered at the air-polymer interface. Continuous gold coverage causes the formation of wrinkles. High coverage and Au nanoparticle (NP) density leads to the development of a spinodal instability while low coverage and NP density retards the nucleation dewetting mechanism that beads up the thin polymer film into drops when no coverage is present. Heating at temperature larger than the polymer glass transition temperature for extended periods allows the gold NPs to coalesce and rearrange. The area of polymer surface covered by NPs decreases as a result and this drives the films from unstable to metastable states.When the gold NPs are interconnected by polymer chains a theoretically predicted spinodal instability that patterns the film surface is experimentally observed. Suppression of the instability and a return to a flat film occurs when the polymer interconnections between particles are broken. While the polymer films maintain their physical continuity changes in their chemical surface composition and thickness are observed. The observed film metastability is nevertheless in agreement with theoretical prediction that includes these surface changes.

## 1. Introduction

Combining thin polymer films with nanoparticles (NPs),[1–5] or thin continuous layers[6–8] of metallic or dielectric materials, can lead to new materials with unique electrical, mechanical, optical or antimicrobial properties for use in devices and coatings. Metallized thin polymer films have many applications ranging from decorations to diffusion barriers in food packaging to dielectric layers in microelectronics.[9] Such films can be produced by vacuum metal deposition that leads to the formation of a discontinuous metal layer of uniformly distributed metal clusters/islands with nanometer dimensions.[9, 10] On amorphous substrates such as polymers, these metal islands are free to diffuse and coalesce on the film surface.[11, 12] These nanometer sized objects are referred to in the present study as nanoparticles.[4,11–13] The particle aggregation process during their diffusion on thin polymer films is relatively well understood,[12] but their influence on the stability of polymer films[1, 4, 5] is still at an early stage.

Thin polymer films on solid substrates become unstable at temperatures larger than the glass transition temperature ($T_g$) and dewet.[14–19] Capping the polymer films with continuous thin layers leads to complex buckling/wrinkling instabilities once above $T_g$,[6–8] while dispersing nanoparticles (NPs) within the polymer matrix can partially suppress dewetting.[1–5] Here, we describe from experimental and theoretical perspectives, how the stability of low molecular weight thin polystyrene (PS) films is controlled by uniformly sputtered gold at the air-polymer interface.

## 2. Theoretical Background

Experimentally, the dewetting process of a thin polymer film starts with the formation of holes that grow and coalesce in time, eventually forming droplets on the substrate. Nucleation and/or spinodal dewetting mechanisms can be responsible for film rupture.[14–18] In the former, dry spots are nucleated by small defects or local thermal fluctuation, while in the latter, spontaneous amplification of the capillary waves occurs.[14–18]

The effective interface potential $\Phi(h)$ determines whether a film is stable, metastable or unstable.[16–18] In the absence of any other external field, the effective interface potential of a thin polymer film placed on a Si substrate covered by a thin $SiO_x$ layer ($h_{SiOx}$), is given by the van der Waals potential:[16, 18]

$$\Phi_{poly} = -\frac{A_{air/poly/SiO_x}}{12\pi h^2} + \frac{A_{air/poly/SiO_x} - A_{air/poly/Si}}{12\pi\left(h + h_{SiO_x}\right)^2} + \Phi_S \quad (1)$$

where $A_{i/j/k}$ are the Hamaker constants describing the interactions between the different layers and the term $\Phi_S = c/h^8$ accounts for the strength of the short-range interactions.[16 – 18]

Thin PS films (> 20 nm thick) on native $SiO_x$ covered Si wafers are metastable and can dewet via nucleation.[16,18] The potential $\Phi(h)$ for such uncovered PS thin films described by equation 1 is shown as curve 1 in **Figure 1**.

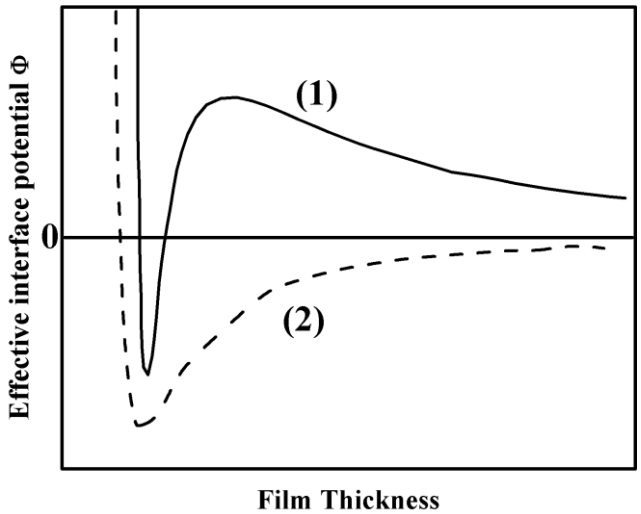


**Figure 1.** Schematic diagram describing the effective interface potential Φ as function of film thickness for (1) metastable and (2) unstable systems.

Provided the potential barrier can be breached, either by thermal fluctuation or the presence of defects, a lower film thickness can be reached, and so the film is conditionally unstable. In contrast, PS films on thicker $SiO_x$[16] can always reduce their energy by simply lowering their thickness (curve 2, **Figure 1**); they are therefore unstable and dewet spinodally. From linear stability analysis of the thin film thickness evolution equation, [17] a spinodal instability can occur when the second derivative of the effective interface potential with respect to the film thickness is negative ($\Phi_{hh}(h) < 0$). In this case, all fluctuations greater than a critical wavelength are amplified, but the maximum growth rate will be associated with a wavelength:

$$\lambda_m = \sqrt{-8\pi^2\gamma/\Phi_{hh}(h)} \qquad (2)$$

where $\gamma$ is the surface tension of the film. The condition $\Phi_{hh}(h) = 0$ marks the transition from unstable to metastable domains for which $\Phi_{hh}(h) > 0$.[14–17]

In films capped by a continuous film of Au,[6–8] the free energy of the system is decreased by the dispersion forces across the film causing instability (similar to curve 2, **Figure 1**) and increased by the free energy associated with the bending of the capping layer.[6–8]

In this study, the intermediate experimental configuration (**Figure 2**) between an uncovered and capped (continuously covered) polymer thin film is investigated i.e. the Au NP covered film in a $Si/SiO_x$/PS/AuNP/Air configuration.

## 3. Materials and methods

### 3.1 Sample preparation

Thin polystyrene films [PS10, $M_w$ = 10 kg/mol, $R_g$ = 2.59 nm, polydispersity index, *PDI* = 1.06, Sigma-Aldrich, UK], of 44, 44, 30, 26 and 30 nm thickness are spin cast from 2 % (w/w) polymer solution in toluene onto Si wafers with a native oxide of $h_{SiOx}$ = 2.0 nm (see **Figure 2a** and **Figure 3a** top left). Prior to spin coating the Si wafers with a resistivity of 2–3 Ω $cm^{-1}$ are cleaned in a jet of $CO_2$ ice crystals. The films are then kept for 24 hours in a closed environment at room temperature to allow the solvent to evaporate.

Gold layers of nominal thickness (i.e. as measured by the crystal monitor system) ~ 0.3, 1, 2, 3 and 10 nm respectively are then sputtered at low deposition rates (~ 0.09 nm $s^{-1}$) in an argon atmosphere at a pressure of 4 × $10^{-3}$ mbar. This creates a $Si/SiO_x$/PS/Au/Air configuration, with the Au forming NPs for $h_{Au}$ ~ 0.3 – 3 nm (**Figure 2b, c and Figure 3a**) and a continuous film for $h_{Au}$ ~ 10 nm (**Figure 2d and Figure 3a**). The polymer film samples are placed horizontally in the vacuum sputtering chamber with the polymer surface pointing to the bottom (i.e. towards the discharge). The polymer films are kept in vacuum for ~ 5 minutes before deposition at ~ 5 × $10^{-8}$ mbar with the sputtering discharge off to ensure the removal of any residual solvent. Prior to each deposition, the gold target is pre-sputtered for 5 – 10 s to remove impurities.

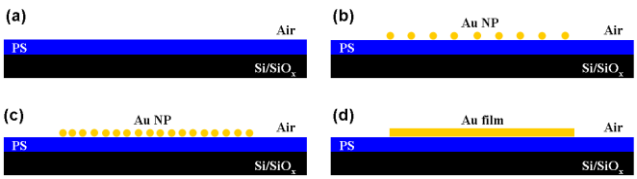


**Figure 2.** Schematic diagram of the samples with (a) no Au coverage, and (b) low, (c) high and (d) continuous coverage obtained after Au sputtering. The samples edges are covered during deposition and only the centre of the samples are covered by Au.

### 3.2 Experimental procedure

The experiments are performed in a classic convection oven in a closed air atmosphere. All samples are heated at 170 ºC, i.e. above the glass transition temperature of the polymer, and are removed and quenched at approximately logarithmically spaced time intervals for optical and SEM analysis.

### 3.3 Optical measurements

We use optical microscopy and software to image surface morphology (see **Figure 3**) and acquire non-contact optical profilometric measurement of roughness over large sample areas.

Optical imaging is performed using a MicroPhase camera (PhaseView, France) placed on a Zeiss AxioImager A1.m microscope. For each time step the optical image is processed using Gwyddion (open source modular software for image analysis funded by the Czech Metrology Institute). The image is enhanced using the plane leveling and adaptive nonlinear color mapping functions. A fast-Fourier-transform (FFT) of the enhanced optical image using FIJI (an Open Source image processing package based on Image J) and an autocorrelation of the raw optical image using Matlab are performed, and the dominant wavelength obtained (see **Figure 4** and **Figure S1** in ESI [20]). The wavelengths measured by FFT of the enhanced image and autocorrelation of the raw image agree within experimental error.

Roughness measurements are made using the MicroPhase camera which provides a 3D visualization with highly repeatable non-contact optical surface profiling capabilities. Roughness, *R*, is the root mean square average of the polymer height deviations and is calculated using

$$R = \sqrt{\sum_i \left(h_i - \bar{h}\right)^2 / N} \ ,$$

where $\left(h_i - \bar{h}\right)$ is the local deviation of the film height from the average value and $N$ is the number of points where the height is measured. The measure of roughness presented in this work (**Figure 5a**) is the roughness value at each time step normalized to the mean value for all time steps. At $t$ = 0 min no significant differences in roughness exist between the Au covered (center) and uncovered (edges) regions of the samples.

### 3.4 Gold characterization

The fractional Au coverage of the PS film ($C_f$ ), the particle number ($N_p$), area ($A_p$), radius ($R_p$), form shape factor ($S_f$ ) and nearest neighbor center to center distance ($d_{cc}$) for all samples in this work are acquired by processing the SEM images of the sample surfaces using SPIP (Image Metrology, AS, Denmark). The form shape factor, $S_f$, is the relative circularity of a Au NP and is given by $S_f = 4\pi A / P^2$, where $A$ and $P$ are the projected area and the perimeter of a NP as seen in and measured from SEM images.[20]

Particles from the SEM images (see **Figure S2** in ESI[20]) are identified and measured using the *"Particles & Pores"* analysis module from SPIP. In this analysis a threshold is applied to each SEM image before processing to distinguish the Au NPs from the effective dielectric charging of electrons on the less conductive polymer. The threshold is selected to be the background intensity level at which all individual particles just become resolved (i.e. where the NP number maximizes). The full scale SEM images, for the nominally 3 nm Au covered sample, when viewed as binary images (0 if less than the threshold and 1 if greater) at $t$ = 7155 min and $t$ = 37395 min reveal a significant reduction in Au coverage (**Figure 5b**) and particle number (see **Figure S3** and **S4** in ESI[20]).

A large reduction in Au coverage is independently verified by angle-resolved X-ray photoelectron spectroscopy (XPS) data (see ESI[20]) which shows a reduction of Au signal by ~60% for the sample on which 1 nm of Au was deposited in good agreement with the SEM analysis (compare with **Figure 5b**).

The XPS measurements confirm that complete embedding of the Au NPs into the polymer is not observed during the experiments. By tilting the sample relative to the normal, the measurements are made more surface sensitive, i.e. as the take-off angle decreases, the sampling depth decreases and near surface regions are probed. The variation in take-off angle allows for a variation in analysis depth from ~ 4.7 nm to ~ 1.6 nm for normal and 20º take-off angle, respectively. Au 4f concentrations of 4.7% versus 2.7% are measured for normal and 20º take-off angles respectively after 37395 min of heating.

## 4. Results

Spin coating of the polymer from solutions on the Si wafer leads to smooth and flat thin polymer films (**Figure 3a**, $h_{Au}$ = 0 nm). As Au is sputtered in the central area of the samples the thin polymer films start to become covered by homogenously and uniform distributed Au nanoparticles (**Figure 3a**, $h_{Au}$ = 0.3 and 3 nm). For a Au nominal thickness of 10 nm, the PS film is covered by a continous layer of gold (**Figure 3a**, $h_{Au}$ = 10 nm). After the Au deposition the polymer films remain smooth and flat as seen by the optical profilometer.

Heating the samples at 170 ºC (well above the glass transition temperarure of the polymer) allows for nucleation driven dewetting to develop in the uncovered thin liquid polymer film (i.e. the samples edges) as expected.[16,17] By the end of the first experimental time step ($t$ = 45 min) the dewetting has reached its final stages, and the polymer is beaded in a Voronoi tessellation pattern of drops (**Figure 3b** left). In stark contrast when the polymer Au coverage is continuous ($h_{Au}$ = 10 nm), the polymer film exhibits clearly defined instability wrinkles (**Figure 3b** right).[6–8] Between these extremes, i.e. for the polymer films covered by Au NPs, we identify two distinct patterns of evolution (**Figure 3c–f**) that are triggered by the (i) sparser ($h_{Au}$ = 0.3 nm) and (ii) denser ($h_{Au}$ = 1, 2 or 3 nm) NP density that corresponds to low and high coverage, respectively.

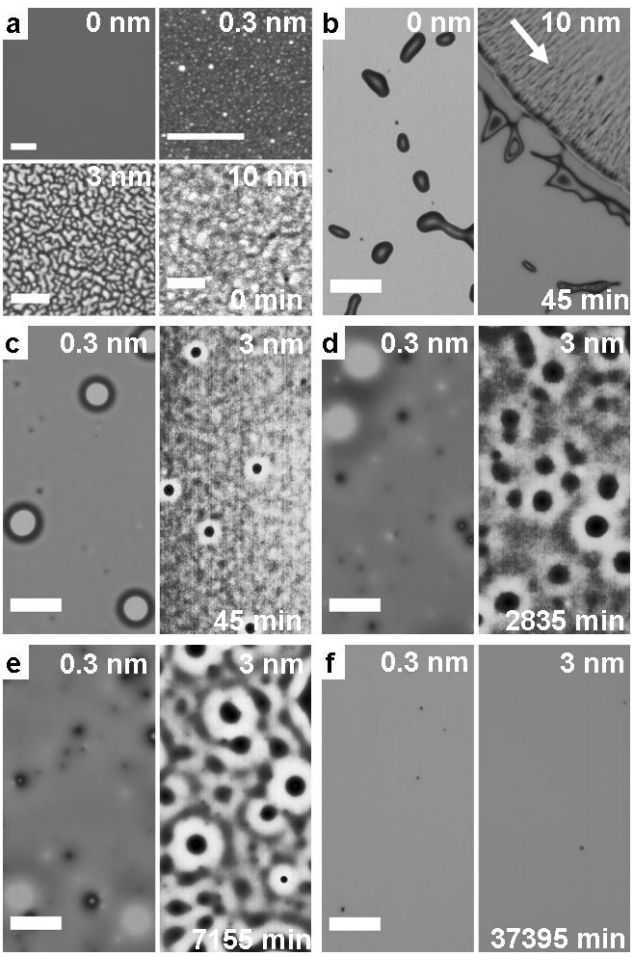


**Figure 3.** (a) Optical image of the uncovered regions (i.e. $h_{Au}$ = 0 nm) at t = 0 min (scale bar 50 μm). AuNP SEM image (scale bar 50 nm) at $t$ = 0 for $h_{Au}$ = 0.3, 3 and 10 nm; (b) Optical images (scale bar 50 μm) for $h_{Au}$ = 0 nm ($h_{PS}$ = 26 nm) and $h_{Au}$ = 10 nm ($h_{PS}$ = 30 nm) at $t$ = 45 min. The white arrow indicates wrinkles; (c) – (f) optical images after different heating times for $h_{Au}$ = 0.3 nm ($h_{PS}$ = 44 nm) and $h_{Au}$ = 3 nm ($h_{PS}$ = 26 nm).

For low coverage, one sees the onset of the nucleation mechanism at $t$ = 45 min (**Figure 3c** left), but this does not develop **(Figure 3d-e** left), and at t = 37395 min the film is flat (**Figure 3f** left). For high coverage, the early stages of a spinodal

instability are observed (**Figure 3c** right) at $t$ = 45 min (see also **Figure S1**). Further heating allows the instability to develop (**Figure 3d** right), and a spinodal pattern is visible at $t$ = 7155 min (**Figure 3e** right). Finally, prolonged heating ($t$ = 37395 min) leads to the suppression of this instability and a return to a flat film (**Figure 3f** right). This makes it unlikely that the instability troughs ever reach the substrate where pinning would lead to permanent holes being formed. All experiments with denser NP coverage i.e. $h_{Au}$ = 1, 2 or 3 nm exhibit similar behavior.

The wavelengths for the $h_{Au}$ = 1, 2 and 3 nm experiments are presented in **Figure 4** as a function of experimental heating time and in each case they obey a power law ($t^{\upsilon}$), with exponents of $\upsilon$ = 0.16, 0.12 and 0.10 respectively. It is recognized that on longer timescales, as instability amplitude increases, roughening modes can develop leading to a larger instability wavelength obeying a $\lambda \sim t^{\upsilon}$ dependence as observed here.[17] Yet, here the exponents are low in comparison to those expected for spinodal decomposition $2/3 \geq \upsilon \geq 1/3$.[17]

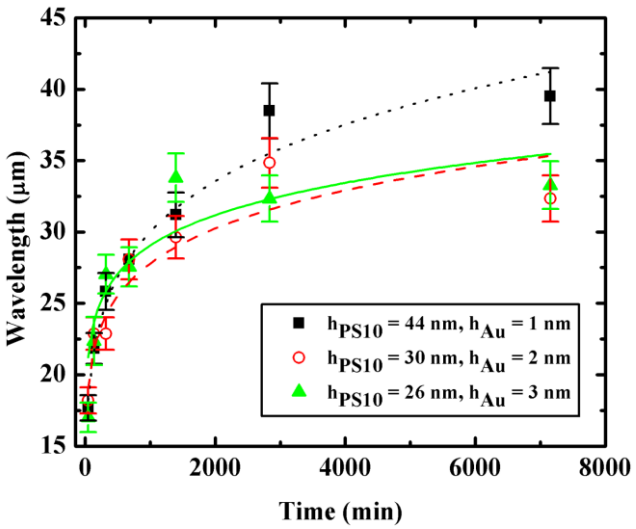


**Figure 4**. The evolution of the measured instability wavelength in time for all three samples exhibiting spinodal instability.

The development and cessation of the spinodal instability are also monitored by measuring the film roughness at each time step. The roughness increases with time reaching a maximum (**Figure 5a**) when the spinodal pattern is developed (**Figure 3e right**) and it is almost completely suppressed after the film surface returns to being flat (**Figure 3f right**).

At $T > T_g$, the Au NPs are mobile and are free to diffuse across the film surface.[10–12, 21 – 23] During their diffusion the NPs tend to aggregate, altering their coverage of the film (**Figure 5b**), and the particle size, shape and number density (**Figure S4** in ESI[20]). The spatial distribution of Au NPs is however always uniformly random independent of the SEM images being acquired on the peaks or within the troughs of the surface instability. Up to t = 7155 min, for the more densely covered films, the coverage increases marginally as the instability develops, but it drops significantly at t = 37395 min when the films become flat (**Figure 5b** and **Figure S2, S3** in ESI[20]). A large drop in Au coverage is independently verified by XPS measurement.[20] For the least densely covered film (i.e $h_{Au}$ = 0.3 nm) the coverage remains approximately constant (**Figure 5b**). It is interesting that the Au NPs never fully embed,[24] but although not explicitly discussed, this effect has been observed previously [10, 13] for similar sample preparation.

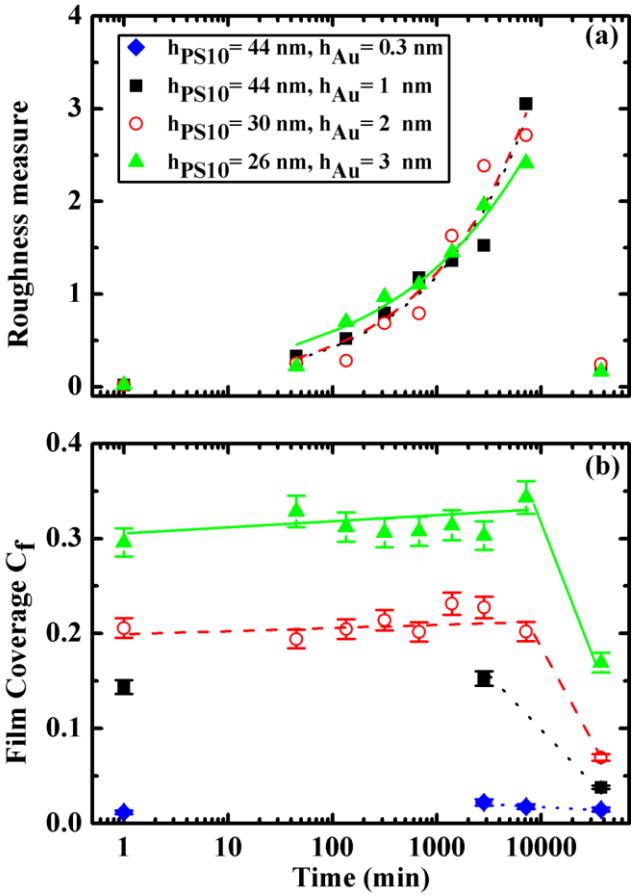


**Figure 5.** (a) The measured polymer film roughness in time obey $t^{\alpha}$ with $\alpha$ = 0.44, 0.44 and 0.33. (b) The Au coverage evolution on the polymer films.

## 5. Discussion

### 5.1 van der Waals interactions

The stability of the Si/$SiO_x$/PS/AuNP/Air system as a function of coverage and particle size can be explored using a simple model in which the total interaction potential between the two interfaces of the system is formed from a combination of $\Phi_{poly}$ ,[16, 18] (Equation 1), and the van der Waals potential for a particle and surface,[25] $\Phi_{AuNP}(h,R_p)$.[20] The relative contributions to the total potential are weighted by the polymer area fraction and particle number density, respectively. The contribution due to short-range interactions is neglected as the polymer films in the present study have thicknesses larger than 20 nm.[16]

The distribution of the NPs is assumed to be uniform and the effect of the polymer-substrate layers beneath a NP is included using the approach of Seemann *et al.*[16]. The total interaction potential is written as:

$$\Phi = (1 - C_f)\Phi_{poly}(h) + p_d \Phi_{AuNP}(h, R_p) \quad (3)$$

where $C_f = p_d \cdot A_p$ and $p_d = N_p/A_{sample}$. By expressing NP number

density $p_d$ and mean radius $R_p$ in terms of fractional coverage $C_f$ and mean NP area $A_p$, the total potential can be written as $\Phi(h,C_f,A_p)$. These relationships show that at low $p_d$ and low $C_f$ the total interaction potential is dominated by $\Phi_{poly}$, while at high $C_f$ the Au NPs dominate.

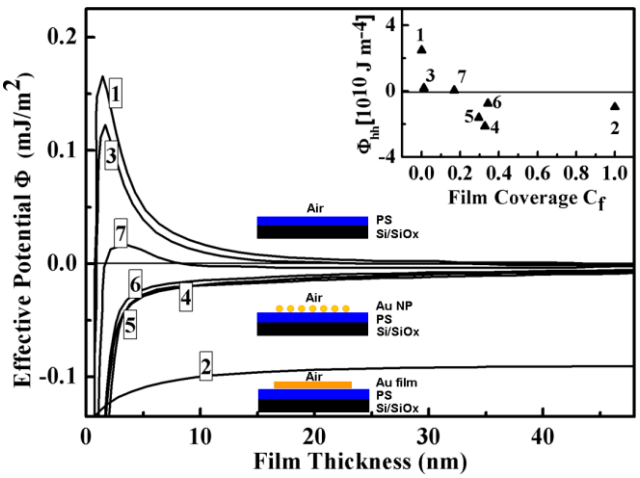


**Figure 6.** The interface potential of a thin PS film for: (1) Si/$SiO_x$/PS/Air, (2) Si/$SiO_x$/PS/Au film/Air ($h_{Au}$ = 10 nm), (3) Si/$SiO_x$/PS/AuNP/Air after heating at $t$ = 0 for $h_{PS}$ = 44 nm with $h_{Au}$ = 0.3 nm and, for $h_{PS}$ = 26 nm with $h_{Au}$ = 3 nm after heating for (4) $t$ = 0, (5) $t$ = 45, (6) $t$ = 7155, and (7) $t$ = 37395 min. Inset: the corresponding values of $\Phi_{hh}(h)$ calculated using the potential curves 1 – 7 as a function of Au coverage ($C_f = A_{Au}/A_{sample}$). For the points (1) and (2) in the inset, the values for $\Phi_{hh}$ are calculated for polymer films with a thickness of $h_{PS}$ = 26 and 30 nm, respectively.

Using equation 1 the potential for a polymer film with no Au coverage is generated. The polymer film is predicted to be metastable (**Figure 6**, curve 1), therefore nucleation dewetting is expected [16 – 18] and is in fact experimentaly observed (**Figure 3b** left). Thin polymer films covered by a continous gold film ($h_{Au}$ = 10 nm) are in contrast expected to be always unstable (**Figure 6**, curve 2) and to exhibit wrinkles; this is also experimentally observed (**Figure 3b**, right).

The effective potential describing the interactions for the Si/$SiO_x$/PS/AuNP/Air system is also presented in **Figure 6** as a function of polymer thickness $h$, for the $h_{Au}$ = 0.3 nm and $h_{Au}$ = 3 nm sample for a number of experimental times using the measured values of $C_f$ and $A_p$. For the more sparsely covered ($h_{Au}$ = 0.3 nm) sample, the model predicts (based on equation 3) that from the outset the system should be metastable (see curve and point 3 in **Figure 6** and its inset). For the densly covered sample ($h_{Au}$ = 3 nm), the model predicts the system to be unstable for $t$ = 0 min (curve 4, **Figure 6**). As the NPs start to aggregate in time, their number density, size and consequently the system coverage change but the system should remain unstable (curves 5 and 6). However in the final stage ($t$ = 37395 min, curve 7) the changes in Au NP size and coverage lead to the formation of a potential barrier and the system should now become metastable. This occurs when the NPs are far apart and the Au coverage is lower. The transition can also be observed in $\Phi_{hh}(h)$ in the inset to **Figure 6**, from instability (points 4 to 6) with $\Phi_{hh}(h)<0$ to metastability (point 7) with $\Phi_{hh}(h)>0$. The model predictions based on equation 3 for both dense and sparse NP coverage are in agreement with experimental observation presented in **Figure 3**.

A stability diagram as a function of the coverage and the mean particle size is presented in **Figure 7a**. It can be seen that for more densely packed NPs the coverage marginally increases over time i.e. during NP aggregation, the mean particle area increases (particle separation also increases) and the system is driven towards the spinodal line.

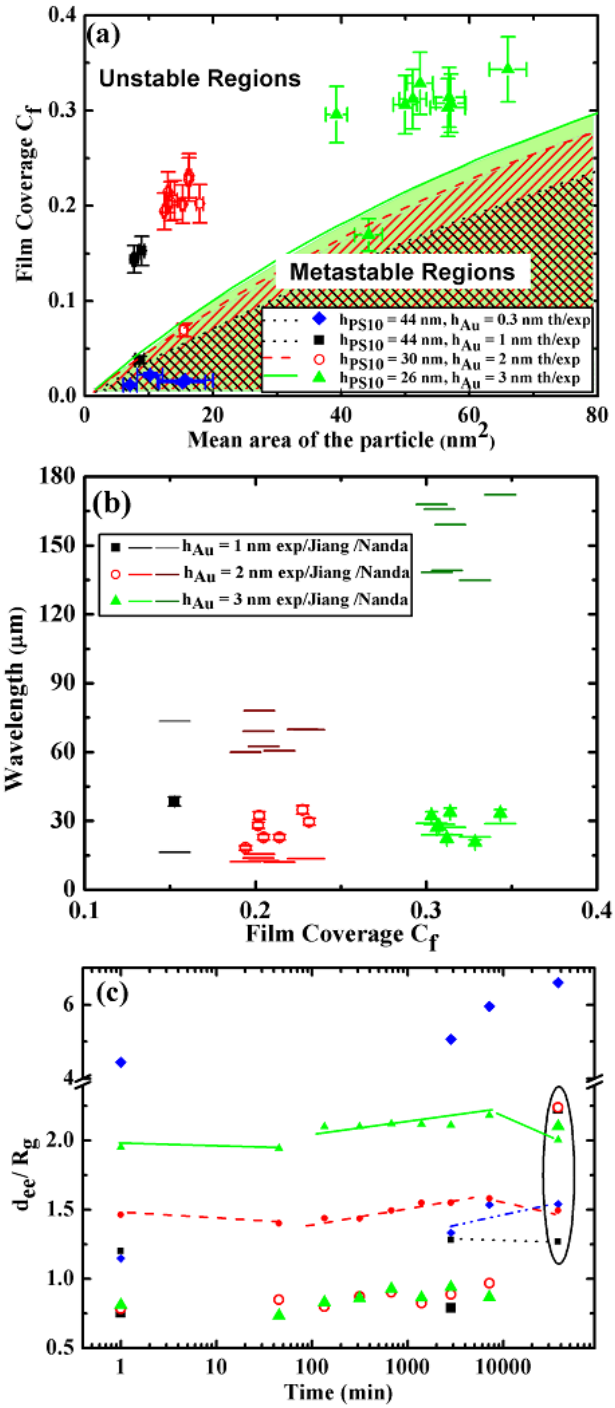


**Figure 7.** (a) Phase diagram describing the transition from unstable to metastable regions (shaded and hatched areas) obtained using the theoretical model and the corresponding experimental data. (b)The experimental and the theoretical predictions of the wavelength. (c) The evolution of the NP edge-to-edge distance $d_{ee}$ (larger symbols) and the connectivity limit $d_m$ (smaller symbols), scaled to the theoretical radius of gyration for PS10.

However, in the final stage of the particle aggregation-rearrangement process, where more spherical particles are well separated, the associated decrease in film coverage ultimately drives the system over the spinodal line into the metastable domain. Thus reduced Au coverage is the main driving mechanism that leads to metastability in the film. This conclusion is supported by the stability trajectory for a sample with sparser NP coverage ($h_{Au}$ = 0.3 nm) which always lies below the spinodal line and is indeed experimentally observed to be metastable from the outset (**Figure 3e-f** left).

The wavelength amplified by the spinodal instability can be estimated using equation 2. The surface tension of the composite polymer nanoparticle system is, to a first approximation, given by $\gamma = C_f \cdot \gamma_{AuNP} + (1 - C_f) \cdot \gamma_{PS}$, where $\gamma_{AuNP}$ and $\gamma_{PS}$ (= 30.8 mJ m$^{-2}$) are the AuNP and the PS surface tension, respectively. As the particles aggregate the coverage changes and, therefore, changes in the surface tension are also expected. For Au NPs the value of the surface tension is still under debate.[24] Therefore, for the wavelength predictions described in **Figure 7b**, the surface tension values were estimated using the theoretical models by Jiang *et al.*[26] and Nanda *et al.*[27] for a solid particle immersed in a fluid of the same composition and for a solid particle in air, respectively. Using these values as limiting cases for the NP surface tension, the theoretical wavelength predictions based on equation 2 bracket the experimental values.

### 5.2 The bridging between the nanoparticles and the existence of a possible capping layer

As the particles aggregate, the coverage decreases, and therefore the distance between particles increases. The measured mean edge-to-edge distance $d_{ee}$ between nearest-neighbor NPs is presented in time in **Figure 7c**. Each $d_{ee}$ is compared with a theoretical bridging limit, defined to be the maximum edge-to-edge separation $d_m$ for which nearest-neighbour NPs remain connected through a polymer chain. The values for $d_m$ can be calculated following the approach of Cole *et al.*[4].

Thus, any polymer chain in contact with more than one NP at a time is defined as being a "bridge". The total number of polymer chains $\psi$ which have at least one segment in contact with a NP can be extracted[4] as a function of the NP radius $R_p$ and the molecular weight of the polymer $M_w$ by

$$\psi_{PS} \cong 5.58R_p + 233M_w^{-1/2}R_p .$$

The average number of NPs which are bound together by bridging molecules is given[4] by $N_n = 2/(2 - \varphi_c(d) \cdot \alpha \cdot \psi)$, where $\varphi_c(d)$ is the local volume fraction of contact chains, and $\alpha$ is the number of NPs at an inter-particle distance $d$ that are available for bridging. Following Ref. [4] and taking $\alpha=1$, the requirement that all NPs are connected by polymer i.e. $N_n = \infty$ is $\varphi_c \cdot \psi = 2$. Knowing the radius of the NPs and, therefore, $\psi$ and $\varphi_c$, we can extract the maximum edge to edge separation $d_m$ for which NPs remain connected from the volume fraction dependence on distance, and radius of the NP (*ibid.* Figure 3 in Ref. [4]).

Comparison with **Figures 3**, **4, 5** and **7a** reveals that for denser NP coverage the system is unstable from $t$ = 0 up to $t$ = 7155 min, which corresponds to times for which $d_{ee} < d_m$, and the Au NPs are interconnected via the polymer. Once this limit is overcome at $t$ = 37395 min and $d_{ee} > d_m$ (to the right of **Figure 7c**) the instability disappears; a flat film is seen in the micrographs (**Figure 3f**) and the roughness diminishes (**Figure 5a**). For sparser NP coverage ($h_{Au}$ = 0.3 nm), the bridging limit is already exceeded from the outset (**Figure 7c**) and the film is both predicted (**Figure 7a**) and observed (**Figure 3c–f left**) to lie within the metastable regime. These results suggest that the thin polymer film stability is related to the bridging limit and/or the resulting NP interconnections.

Confinement of the polymer chains[28] between NPs when $d_{ee} < d_m$ might lead to an increase in $\gamma_{PS}$, but such an increase can only affect the instability wavelength, and would be a minor contribution as $\gamma$ is dominated by $\gamma_{AuNP}$. An alternative is that an effective capping layer is created by the network of NPs when interconnected. Such a nanocomposite layer would have a maximum thickness of $t_{nc} = 2R_p + d_m$. Following Ref. [8], one can show the instability growth rate for an effectively capped polymer film, $\beta$, for wavenumber, $k$, is given by $\beta/C = -D \cdot k^6 - \gamma_{int} \cdot k^4 - \Phi_{hh} \cdot k^2$, where $D$ is the flexural rigidity of the capping layer, $\gamma_{int}$ is the interfacial tension between it and the underlying polymer, $\Phi$ is given by equation 3 and $C$ depends on polymer mobility. While $\gamma$ and $D$ are unknown, the condition for instability growth i.e. $\beta > 0$ remains unchanged from that presented in **Figure 7a**, namely $\Phi_{hh} < 0$. Therefore, only the wavelength of the instability can depend on $D$ and $\gamma_{int}$. Instead, it may be that the aggregation and rearrangement of the NPs which determine $p_d$ and $C_f$ , the determining factors in $\Phi_{hh}$, are affected by the connections bridging the NPs via the polymer chains. Polymer bridged NPs are thought to diffuse as an aggregate,[4, 29] leading to much lower rates of diffusion, and this is consistent with experimental observation here. The diffusion constant $D_{NP}$ can be estimated using the change in the edge-to-edge separation $\Delta d_{ee}$ that occurs over a time interval $\Delta t$, such that $\Delta d_{ee} \sim (D_{NP} \cdot \Delta t)^{1/2}$. Comparing the later stage separations at 7155 min with those at 45 min, the estimated Au NP diffusion constants are found to be remarkably small (typically ~ $10^{-26}$ m$^2$/s for the 2 and 3 nm samples).

Given that the samples were heated in air over extended periods (37395 min), it is important to consider the physical and the chemical changes that might occur in the polymer films and their influence on the formation of the polymer instability. Changes to the film do occur, film thickness reduces (possibly due to polymer degradation and/or polymer densification[30] as a result of adhesion to the Au[31]), and oxygen is present at the film surface due to plasma deposition process and heating. Allowing for a reduced film thickness and revised Hamaker constants to include the oxygen, and using the model in equation 3, changes the spinodal curve in the stability diagram, but the experimentally observed instability and metastability remain correctly predicted (see ESI[20] for a detailed discussion). Indeed, from the outset i.*e. prior to extended heating* the sparse NP or low Au coverage sample is predicted via equation 3, and experimentally observed, to be metastable as a consequence of the lower Au NP coverage.

The importance of particle coverage in film stabilization is also supported by the observation that increasing fractional coverage of polystyrene particles segregated to the polymer-substrate interface retards nucleation dewetting.[32] There, however, it is the

increase in the domination of the short-range repulsive interactions with coverage that leads to the increased stability rather than the changes in the long-range van der Waals potential, and the spinodal to metastable transition is not observed.

## 6. Conclusions

In conclusion, it has been shown both experimentally and theoretically that the stability of a polymer film covered by uniformly distributed NPs is influenced by the area of coverage and the particle number density at the polymer-air interface from the outset. Continuous coverage leads to wrinkle formation, large coverage and NP density leads to the development of a spinodal instability while low coverage and NP density retards the nucleation dewetting mechanism that beads up the thin polymer film into drops when no coverage is present. The theoretical model presented here captures the formation of an energy barrier and the transition of the system from unstable to metastable regimes. Estimations of the instability wavelength based on this model bracket the experimental findings well. It is posited that when the mean edge-to-edge distance $d_{ee}$ between NPs is smaller than the bridging limit $d_m$, the NPs are in close proximity to each other and have a collective influence on the polymer film. When the distances between the NPs are large we expect that the Au NPs have only individual, local influence on the polymer film. The importance of $d_{ee}$ as a controlling parameter in the development of the instability can be verified using polymers of different molecular weight, and will be explored in the future using X-ray reflectivity. These measurements will also offer the possibility of studying changes in the polymer chains density and in the interconnections between Au NPs, to establish the exact relationship between polymer chain confinement and instability appearance and disappearance.

**Acknowledments**

We thank Prof. U. Steiner and Prof. U. Thiele for helpful suggestions and discussions on this work. We acknowledge support under EU Framework 7 for projects MRTN-CT-2004005728 (PATTERNS) and PERG04-GA-2008-239426 (POLYPATT), and from the Tyndall National Institute through the Science Foundation Ireland funded National Access Programme (Project NAP200). This work was also supported by Science Foundation Ireland under contract no.07/SK/B1232a.

## Notes and references

[a] *Department of Physics and Energy, University of Limerick, Ireland. Fax: +353 61 202423; Tel: +353 61 202625; E-mail: george.amarandei@ul.ie*
[b] *Department of Chemistry, University College Cork,Cork, Ireland*
[c] *Tyndall National Institute, Lee Maltings, Cork, Ireland*

Electronic Supplementary Information (ESI) available: [details of any supplementary information available should be included here]. See DOI: 10.1039/b000000x/

1 H. C. Wong and J. T. Cabral, *Phys. Rev. Lett.*, 2010, **105**, 038301
2 H. C.Wong and J. T. Cabral, *Macromolecules*, 2011, **44**, 4530
3 K. A. Barnes, A. Karim, J. F. Douglas, A. I. Nakatani, H. Gruell, and E. Amis, *Macromolecules*, 2000, **33**, 4177
4 D. H. Cole, K. R. Shull, P. Baldo, and L. Rehn, *Macromolecules*, 1999, **32**, 771
5 R. Mukherjee, S. Das, A. Das, S. K. Sharma, A. K. Raychaudhuri, and A. Sharma, *ACS Nano*, 2010, **4**, 3709
6 K. Dalnoki-Veress, B. G. Nickel, and J. R. Dutcher, *Phys. Rev. Lett.*, 1999, **82**, 1486
7 G. A. Buxton and N. Clarke, *Phys. Rev. E*, 2006, **74**, 041807
8 P. J. Yoo, K.Y. Suh, H. Kang, and H. H. Lee, *Phys. Rev. Lett.*, 2004, **93**, 034301
9 G. Kaune, M.A. Ruderer, E. Metwalli, W. Wang, S. Couet, K. Schlage, R. Röhlsberger, S. V. Roth, and P. Müller-Buschbaum, *ACS Appl. Mater. Interfaces*, 2009, **1**, 353
10 M. Z. Kunz, K. R. Shull, and A. J. Kellock, *J. Appl. Phys.*, 1992, **72**, 4458
11 W.A. Lopes and H. M. Jaeger, *Nature*, 2001, **414**, 735
12 W. A. Lopes, *Phys. Rev. E.*, 2002, **65**, 031606
13 R. L. W. Smithson, D. J. McClure, and D. F. Evans, *Thin Solid Films*, 1997, **307**, 110
14 G. Reiter, *Phys. Rev. Lett.*, 1992, **68**, 75
15 R. Xie, A. Karim, J. F. Douglas, C. C. Han, and R. A. Weiss, *Phys. Rev. Lett.*, 1998, **81**, 1251
16 R. Seemann, S. Herminghaus, and K. Jacobs, *Phys. Rev. Lett.*, 2001, **86**, 5534
17 U. Thiele, Thin films of Soft Matter (Springer, Wien, 2007), chap. Structure formation in thin liquid films
18 O. Baeumchen and K. Jacobs, *J. Phys-Cond. Matt.*, 2010, **22**, 033102
19 J. P. de Silva, M. Geoghegan, A. M. Higgins, G. Krausch, M. O. David, and G. Reiter, *Phys. Rev. Lett.*, 2007, **98**, 267802
20 G. Amarandei, See supplementary material in ESI
21 A. Gopinathan, *Phys. Rev. E.*, 2005, **71**, 041601
22 X. Jia, J. Listak, V.Witherspoon, E. E. Kalu, X. Yang, and M. R.Bockstaller, *Langmuir*, 2010, **26**, 12190
23 M. Jose-Yacaman, C. Gutierrez-Wing, M. Miki, D. Q. Yang, K. N. Piyakis, and E. Sacher, *J. Phys. Chem. B.*, 2005, **109**, 9703
24 R. D. Deshmukh and R. J. Composto, *Langmuir*, 2007, **23**, 13169
25 J. Israelachvili, *Intermolecular and Surface Forces*, Academic Press, London 1992
26 Q. Jiang, L. H. Liang, and D. S. Zhao, *J. Phys. Chem. B.*, 2001, **105**, 6275
27 K. K. Nanda, A. Maisels, F. E. Kruis, H. Fissan, and S. Stappert, *Phys. Rev. Lett.*, 2003, **91**, 106102
28 T. Sakaue and E. Raphaël, *Macromolecules*, 2006, **39**, 2621
29 J. Liu, D. Cao, and L. Zhang, *J. Phys. Chem. C*, 2008, **112**, 6653
30 S. Napolitano and M. Wubbenhorst, *Nature Communications*, 2011, **2**, 260
31 T. Fu, U. Stimming, and C. Durning, *Macromolecules*, 1993, **26**, 3271
32 R. S. Krishnan, M. E. Mackay, P. M. Duxbury, C. J. Hawker, S. Asokan, M. S. Wong, R. Goyette, and P. Thiyagarajan, *J. Phys. Condens. Mat.*, 2007, **19**, 356003